Quantum dynamics of a single molecule magnet on superconducting Pb(111) / Serrano, G.; Poggini, L.; Briganti, M.; Sorrentino, A. L.; Cucinotta, G.; Malavolti, L.; Cortigiani, B.; Otero, E.; Sainctavit, P.; Loth, S.; Parenti, F.; Barra, A. -L.; Vindigni, A.; Cornia, A.; Totti, F.; Mannini, M.; Sessoli, R.. - In: NATURE MATERIALS. - ISSN 1476-1122. - 19:5(2020), pp. 546-551. [10.1038/s41563-020-0608-9]

Accepted manuscript of: Serrano, G., Poggini, L., Briganti, M. et al. Quantum dynamics of a single molecule magnet on superconducting Pb(111). Nat. Mater. 19, 546–551 (2020).
https://doi.org/10.1038/s41563-020-0608-9
https://www.nature.com/articles/s41563-020-0608-9

Quantum Dynamics of a Single Molecule Magnet on Superconducting Pb(111)

Giulia Serrano[1,2*], Lorenzo Poggini[1], Matteo Briganti[1], Andrea Luigi Sorrentino[1,2], Giuseppe Cucinotta[1], Luigi Malavolti[3], Brunetto Cortigiani[1], Edwige Otero[4], Philippe Sainctavit[4,5], Sebastian Loth[3], Francesca Parenti[6], Anne-Laure Barra[7], Alessandro Vindigni[8], Andrea Cornia[6], Federico Totti[1], Matteo Mannini[1] and Roberta Sessoli[1*]

1. *Department of Chemistry "Ugo Schiff" and INSTM Research Unit, University of Florence, 50019 Sesto Fiorentino, Italy. roberta.sessoli@unifi.it*
2. *Department of Industrial Engineering and INSTM Research Unit, University of Florence, 50139 Florence, Italy. giulia.serrano@unifi.it*
3. *Max Planck Institute for Solid State Research and University of Stuttgart, 70569 Stuttgart, Germany*
4. *Synchrotron SOLEIL, L'Orme des Merisiers, Saint Aubin BP48 91192 Gif-sur-Yvette Cedex, France*
5. *IMPMC, UMR7590 CNRS, Sorbonne Université, MNHN, 75005 Paris, France*
6. *Department of Chemical and Geological Sciences and INSTM Research Unit, University of Modena and Reggio Emilia, 41125 Modena, Italy*
7. *LNCMI-CNRS, Univ. Grenoble-Alpes, 38042 Grenoble Cedex 9, France*
8. *Laboratorium für Festkörperphysik, ETH Zürich, Zürich, Switzerland*

Abstract

Magnetic materials interfaced with superconductors may reveal new physical phenomena with potential for quantum technologies. The use of molecules as magnetic components has already shown great promise, but the diversity of properties offered by the molecular realm remains largely unexplored. Here we investigate a sub-monolayer of tetrairon(III) propeller-shaped single molecule magnets deposited on a superconducting lead surface. This materials combination reveals a strong influence of the superconductor on the spin dynamics of the single molecule magnet. It is shown that the superconducting transition to the condensate state switches the single molecule magnet from a blocked magnetization state to a resonant quantum tunnelling regime. Our results open perspectives for controlling single molecule magnetism via superconductors and for using single molecule magnets as local probes of the superconducting state.

Interfaces between superconducting and ferromagnetic materials are widely investigated for the richness of the novel physical phenomena they exhibit, which hold great potential in spintronics and quantum information technologies.[1] Among them, infinite magnetoresistance was observed in spin-valves embedding superconducting layers between ferromagnetic electrodes.[1] The intercalation of a ferromagnetic layer in a Josephson junction introduces a tunable phase shift allowing control of quantum circuits.[1]

As far as molecular spins are concerned, scanning tunnelling spectroscopy in the proximity of flat paramagnetic molecules deposited on ultrathin superconducting layers provided examples of local quasiparticle excitations within the superconducting gap, giving rise to localized magnetic states known as Yu−Shiba−Rusinov (YSR) bound states.[2–4] Monolayers of paramagnetic molecules can also influence the critical temperature of a thin superconducting layer,[3,5,6] and exhibit increased spin lifetimes on superconducting bulk crystals.[7] However, the use of a superconducting substrate to manipulate the magnetism of molecular magnets is, to the best of our knowledge, unexplored.

Among molecular magnets, molecules showing a directionally bistable magnetic moment are known as single molecule magnets (SMMs). They combine a large molecular spin with an easy-axis magnetic anisotropy, which leads to an energy barrier opposing to the reversal of the magnetization.[8] Moreover, quantum phenomena in the spin dynamics make this class of nanomagnetic objects very appealing for spintronics and quantum computing.[9] Notably, Grover's algorithm has been implemented on a single nuclear spin by embedding a SMM in a nanojunction.[10]

SMMs allowing the realization of a well-defined molecule-superconductor hybrid interface are limited. Tetrairon(III) complexes[11] (Fe_4) with a propeller shape (Figure 1a) constitute one of the few families of SMMs that have been studied in detail when deposited on a metallic substrate.[12–15] Hybrid interfaces were obtained from solution,[12,13] as well as via thermal sublimation in ultra high vacuum (UHV) conditions.[14] In both cases, at variance with other SMM complexes,[16–19] the magnetic bistability was found to persist at sub-monolayer coverage thanks to the efficient protection of the magnetic core exerted by the ligand shell.

Here we report the investigation of a sub-monolayer of Fe_4 SMMs on lead, a type I superconductor. We studied the structural and chemical properties of the Fe_4 monolayer by combining scanning tunnelling microscopy (STM) with photoelectron spectroscopies flanked by density functional theory (DFT) calculations. We employed X-ray magnetic circular dichroism (XMCD) to observe the magnetic fingerprint of the molecular layer and investigate its magnetic hysteresis on the superconductive substrate. The results show that the magnetization dynamics of the SMMs is influenced by the superconductive (SC) transition to the condensate state.

Fe_4SMe on Pb(111): surface preparation and characterization

<<< INSERT FIGURE 1 SINGLE COLUMN AROUND HERE >>>

In the structure of Fe_4 SMMs, $[Fe_4(L^R)_2(dpm)_6]$, the magnetic core is held together by tripodal ligands $(L^R)^{3-}$ = $[RC(CH_2O)_3]^{3-}$ located on either side of the molecular plane, whereas dipivaloylmethanido ligands (dpm^-) are found at the periphery (Figure 1a).[11] The bridging oxygen atoms of the tripods promote antiferromagnetic interactions between the $s = 5/2$ spins of central and peripheral Fe^{3+} ions. The resulting ground state has total spin $S = 5$ and is well separated (ca. 55-65 K[20]) from the excited $S = 4$ states. The ground manifold is dominated by a moderate uniaxial magnetic anisotropy, $\widehat{H}_{an} = D\hat{S}_z^2$, along the idealized C_3 molecular axis (z), which is oriented normal to the molecular plane. The anisotropy is of the easy-axis type with $D/k_B \sim -0.6$ K and creates an energy barrier $|D/k_B|S^2 \sim 15$ K. Magnetic bistability is thus observable in the hysteresis loops only at temperatures below 1 K. The loops present the butterfly shape typical of resonant quantum tunnelling of the magnetization (QTM) in zero field.[8]

As a key feature, Fe_4 complexes can be tailored by proper choice of R substituent on tripodal ligands while only marginally affecting magnetic properties. With R = Ph the molecules sublimate in UHV conditions but the bulky Ph group limits the formation of perfectly ordered monolayers.[14] On the contrary, Fe_4 SMMs with R = H, deposited using electrospray, adopt a flat adsorption geometry (*i.e.* with the plane defined by the Fe atoms parallel to the surface) and form an ordered hexagonal layer.[21–23]

After careful screening of alternative substituents, we found that when R = CH_2SMe (see tripodal ligand in Figure 1a), the Fe_4 complex is compact enough to warrant the formation of a well ordered 2D lattice but also presents the necessary thermal stability to allow sublimation. The synthesis of the new proligand H_3L^{CH2SMe} and of its tetrairon(III) complex (Fe_4SMe hereafter), are described in the Supplementary Note 1. Structural characterization by X-ray diffraction (see Supplementary Note 2) revealed the typical pseudo-three-fold symmetry. Characterization of the magnetic properties by DC and AC methods, flanked by high-frequency electron paramagnetic resonance (EPR) spectroscopy, confirmed the dominating uniaxial magnetic anisotropy with spin Hamiltonian parameters in line with other derivatives of the same family (see Supplementary Note 3).

A Pb single crystal exposing the (111) face was selected as the substrate for molecular deposition. Lead behaves as a superconductor below the critical temperature (T_C) of 7.2 K and critical field (B_C) of 0.08 T.[24] In this field region, Fe_4 SMMs display enhanced magnetic bistability because resonant quantum tunnelling is suppressed.

Molecules were deposited by thermal sublimation on a clean Pb(111) surface to obtain a sub-monolayer coverage (see Methods). Different magnifications of STM images of the molecular film are reported in Figure 2. Islands of Fe_4SMe molecules partially cover the Pb surface. They show a highly ordered hexagonal pattern with a periodicity of 1.7(2) nm. A detailed analysis of the STM height profiles before and after molecular deposition is provided in the Supplementary Note 4. Different orientations of Fe_4SMe molecular pattern, specifically addressed in Extended Data Fig. 2a, are observed and locally produce disordered areas at the borders of adjacent islands. The steric hindrance of the CH_2SMe group produces a tilted adsorption geometry (similarly to complexes with R = $(CH_2)_5SAc$ and Ph on Au[13,14]). A closer look at the molecular layer (Figure 2b) indicates the presence of a superstructure of triangles formed by three molecular units. Triangles are packed with opposite orientation in a double row, or in a single row (Extended Data Fig. 2b).

In order to better understand the STM observations, we investigated the Fe_4SMe/Pb(111) interface by theoretical methods. One single Fe_4SMe molecule was optimized at the periodic DFT level of theory (see Methods). In the relaxed geometry, the idealized three-fold axis (see Figure 1b) forms an angle $\Omega \sim 22°$ with the surface normal (n). This configuration is driven by van der Waals interactions of the Pb atoms with the sulphur atom and with the hydrogen atoms of two dipivaloylmethanido ligands positioned close to the surface. Moreover, DFT foresees a preferred atop interaction of S with a Pb atom, which is extracted by ca. 0.9 Å from the top layer. Calculations evidence a low adsorption energy thus suggesting a physisorption process, being the lysis of the S-Me bond sterically hindered.[25]

<<< INSERT FIGURE 2 DOUBLE COLUMN AROUND HERE >>>

The superstructure observed in the STM images can be reproduced through DFT modelling by taking into account three closely packed molecular units and allowing the structure to relax (see Methods). Extended Data Fig. 2d shows the minimum energy configuration where molecules retain their easy axes at 22° with the surface normal, and the easy-axis projections on the surface are arranged at 120° intervals. The simulated STM image of this structure (Figure 2d) well reproduces the observed triangular features.

A chemical analysis of the Fe_4SMe/Pb(111) surface performed by X-ray photoelectron spectroscopy (XPS) confirmed the integrity of the molecular layer after the deposition process (see Supplementary Note 5). The electronic structure of the molecular film was studied by ultra-violet photoelectron spectroscopy (UPS), see Supplementary Note 6. The shape of the He(II) spectrum (see Supplementary Figure 10) is compatible with literature reports on layers of similar Fe_4

complexes.[26] Furthermore, the comparison of the UPS spectrum with the corrected total density of states (c-TDOS) and with the single-element contributions of the molecules to the TDOS allowed a careful assignment of each spectral feature. Projected density of states (pDOS) provided more insights on the molecule/surface interaction. Being the Fermi region of relevance for superconductivity, we notice that the filled 3*d* bands (alpha component) of the iron ions extend from -9 up to -1 eV with respect to the Fermi energy, E_f, while the empty ones are right above E_f (see Extended Data Fig. 1b and Supplementary Note 7). Contributions of S, C, and O orbitals are also present in the range $E_f \pm 1$ eV (see Extended Data Fig. 1b). To reveal any possible molecule-substrate hybridization, we computed the electron density difference between Fe_4SMe/Pb(111) and its separated components (Fe_4SMe and Pb substrate). Figure 1b shows that the largest difference is observed for the displaced Pb atom and the CH_2SMe group; this indicates formation of a non-negligible covalent Pb-S interaction, leading to weak electronic hybridization. However, the spin density computed for the Fe_4SMe/Pb(111) interface (see Extended Data Fig. 1b) reveals no sizeable spin delocalization on the Pb atoms. This result indicates that the ligand shell efficiently shelters the Pb surface from the Fe^{3+} ions.

Magnetic characterization of the molecular film

The magnetic characterization of the Fe_4SMe sub-monolayer on Pb(111) was carried out using X-ray synchrotron light and a ^3He-^4He dilution refrigerator to access the mK temperature range (see Methods).[27] X-ray absorption spectra (XAS) were measured at the Fe $L_{2,3}$ edges with the X-ray beam directed parallel to the applied magnetic field (B) and forming a variable angle θ with the surface normal (see inset in Figure 3d). Spectra were acquired at B = 3 T and T = 220 mK (nominally the lowest reachable temperature at the sample holder). At normal incidence ($\theta = 0°$) XAS spectra obtained with positive (σ^+, red) and negative (σ^-, blue) circular polarization show the expected shape for a Fe_4 complex (Figure 3a).[12–14] The normalized XMCD signal (see Methods) shows a dominant negative peak at 709.2 eV with an intensity of about 40%. The intensity and line shape are distinctive of Fe_4 complexes, being a fingerprint of the antiparallel alignment of nearest-neighbouring spins in the ground state (Figure 1a).[12–14,28] A slightly lower intensity (~37%) is observed at $\theta = 45°$ (Extended Data Fig. 3a), as expected for molecules with the preferential orientation suggested by STM images and DFT calculations.

X-ray natural linear dichroism (XNLD) was used to further assess molecular orientation at the Pb(111) surface. The XNLD spectrum (Figure 3b) is dominated by a dichroic signal at 709.2 eV, whose amplitude (about 6%) is greater than found in other monolayers of Fe_4 complexes.[13] It confirms a more pronounced alignment of the molecules, in line with STM and DFT findings.

The dynamics of the magnetization of the Fe_4SMe layer on Pb(111) was studied at normal incidence ($\theta = 0°$) in the temperature range from 220 mK to 900 mK (Figure 3c) by monitoring the XMCD signal at its maximum intensity while sweeping the magnetic field in a continuous mode. At 900 mK the hysteresis loop is practically closed; it opens progressively upon cooling and becomes almost temperature independent below 500 mK. This behaviour is typical of Fe_4 SMMs at the cross-over from a thermally activated relaxation mechanism to a tunnelling regime.[29]

<<< INSERT FIGURE 3 DOUBLE COLUMN AROUND HERE >>>

Magnetic hysteresis was also studied as a function of the incidence angle θ at 220 mK (Figure 3d). The hysteresis curves are characterized by efficient QTM at zero field ("butterfly shape"), as found in other monolayer deposits of Fe_4 complexes.[13,14] At normal incidence, the hysteresis closes rather abruptly at about ±0.45 T in correspondence to the first field-induced level crossing, *i.e.* where the $m_S = \pm 5$ and $m_S = \mp 4$ levels are degenerate, and QTM is enhanced.[11,30] By contrast, at $\theta = 45°$ we observe a gradual change of the magnetization from 0.45 T to 0.70 T. Geometrical arguments can explain this finding. According to DFT results, molecular easy axes are tilted by $\Omega \sim 22°$ from the surface normal and, in first approximation, distributed on the surface of a cone. While at $\theta = 0°$ the first level crossing occurs at the same field for all molecules, at $\theta = 45°$ the angle between the external field and the molecular easy axis spans the interval $45° \pm \Omega$, *i.e.* from 67° to 23°. Since level crossing moves to higher fields with increasing angles, the hysteresis closes over a wider field range.

Simulation of the hysteresis loops

Simulation of the Fe_4SMe magnetic hysteresis was performed starting from the spin Hamiltonian of the ground $S=5$ state and computing the transition probabilities between the different sublevels.[13] Thermally-activated processes were treated considering the spin-phonon coupling explicitly, within the approximations presented in Ref. 8. An additional heuristic term was added to the transition rates to account for pure tunnelling between almost degenerate levels (see Supplementary Note 8). The resulting master equation was integrated using the kinetic Monte Carlo method to evaluate the time-dependent magnetization. The use of (variable-step) kinetic Monte Carlo, based on stochastic time increments, has the advantage of providing comparable accuracy with less computational resources compared to previously employed direct integration.[13] The latter, indeed, requires an appropriate *a priori* choice of the integration (fixed) time step.

Hysteresis loops were simulated by placing the molecular easy axes at 22° from the surface normal and optimizing the spin Hamiltonian parameters to the values reported in the Supplementary Note 8. The close agreement of the simulated and experimental curves over the whole temperature range here explored (see Figure 3c) indicates the reliability of this approach. Differences in the hysteresis loop for different incidence angles (Figure 3d) are also nicely reproduced.

SMMs dynamics inside the superconducting window of lead

We now focus on the dynamics of the magnetization of Fe_4SMe in the field range in which the substrate is superconductor ($|B| < B_C$). Figure 4a shows an enlargement of the low field region of the hysteresis loop at $\theta = 0°$ and 220 mK (green circles), acquired at a lower field sweep rate (0.0025 T/s) in order to increase the data resolution. Starting from high fields, when the applied field enters in the SC window ($B < B_C$) the XMCD signal decreases, deviating significantly from the predicted squared behaviour around zero field (black line) and from the observed response of similar complexes on non-superconductive substrates[27] (a detailed comparison is available in Extended Data Fig. 4a). It can be noticed that the noise level in the experimental data increases significantly when the applied field exits from the SC window. Rapid variations of the magnetic induction around zero field are known to affect the efficiency of the photoelectrons leaving the sample and thus to influence the signal detection in the TEY mode (see Methods). Flux noise effects were also detected in SC circuits and attributed to the presence of O_2 molecules.[31,32] However, a possible explanation for the observed asymmetry of the noise is that the magnetic induction of the molecular film has a mitigating effect on the photoelectrons. When the substrate enters the SC phase, the molecular layer is fully magnetized, and its magnetization gradually vanishes towards zero field. As the field is reversed and exits the SC window, the molecular layer is fully demagnetized, leading to an abrupt change in the local induction felt by the photoelectrons.

<<< INSERT FIGURE 4 DOUBLE COLUMN AROUND HERE >>>

To minimize the noise, the XAS signal was recorded by switching the X-ray polarization at each sampled magnetic field. The field was ramped back to 1 T before measuring each point of the hysteresis in order to maintain a sweep rate similar to the continuous mode. The blue circles in Figure 4a represent the hysteresis data acquired in this “spot” mode. Also in this case, the Fe_4SMe magnetization decays below B_C, clearly evidencing that the SMMs in the monolayer experience the local field (B_{loc}) generated by the superconductor.

The approximately linear decrease of the magnetization observed below B_C is in agreement with the transition of a type I superconductor to the intermediate state. In this state SC and normal (N) regions coexist in the metal.[33] In a simplified model, *i.e.* assuming a demagnetization factor equal to one, the SC fraction (f_S) increases linearly by lowering $|B|$ according to $f_S \sim 1\text{-}|B|/B_C$.[33] Regions of the superconductor entering the complete Meissner state (light grey areas in Figure 4b) expel the applied magnetic field, pushing the field flux lines in the neighbouring N regions (dark grey in Figure 4b), where the magnetic field is pinned to the B_C value.[33] The relative amounts of SC and N regions vary with the applied magnetic field, as sketched in Figure 4b. Thus, each region of the superconductor experiences the transition to the Meissner state at different values of the applied field, ranging from B_C to zero field.

This scenario is expected to represent also our experimental conditions. Magneto-optical studies, indeed, revealed the presence of the intermediate state in disk-shaped lead crystals with similar size to ours.[34,35] The topology of the domains depends on the shape of the sample and the applied magnetic field. Their dimension ranges from micrometric to sub-mm size.[34,35] Being the size of the X-ray spot about 1 mm in diameter, the XMCD signal averages the response of SMMs lying on N and SC regions.

For $B < B_C$, SMMs experience a B_{loc} generated by the superconductor: those in the proximity of a normal region feel $B_{loc} \sim B_C$ until that region enters into the Meissner state, B_M being the applied field at which this occurs. At this point, the molecules suddenly feel a local field $B_{loc} \sim 0$, and magnetic relaxation by QTM becomes possible.

To reproduce the hysteresis curve, we simulated a set of hystereses assuming different B_M values (Figure 4c), so as to describe SMMs that feel an abrupt transition from B_C to zero field at different times during the field scan. Taking into account the fractions of the substrate that experience different B_M values, and assuming a homogenous distribution of SMMs on the surface, we obtained the hysteresis curve shown as a red line in Figure 4a. In the SC window, the demagnetization of the Fe_4SMe layer is calculated to occur linearly with the field, in good agreement with the experimental data. It is also interesting to analyse the branch of the hysteresis measured by increasing the field amplitude but with opposite polarity. Both experimental and calculated curves are close to zero. Indeed, Fe_4SMe SMMs cannot be magnetized when the underlying Pb region exits the Meissner state, and the local field switches back to B_C. At this field, resonant quantum tunnelling is suppressed, and the magnetization is practically blocked over the time scale of the hysteresis. The absence of a linear trend in this portion of the hysteresis allows excluding the presence of species behaving like normal paramagnets.

Outlook

The unprecedented combination of two materials, which are archetypes of two very different classes, *i.e.* superconductors and SMMs, has here provided the proof of principle of a novel mechanism for SMMs magnetization switching and SC sensing. The formation of the intermediate state in a type I superconductor induces the transition of Fe_4SMe SMMs from the blocked magnetization to the resonant quantum tunnelling regime. Such a transition is promoted by the external field cancellation associated with the Meissner effect.

Fundamental for this achievement were (i) the chemical design of an evaporable Fe_4 SMM forming an ordered monolayer on the Pb substrate and (ii) the observation of hysteresis curves at sub-kelvin temperatures by XMCD. It is noteworthy that this surface-sensitive technique has been seldom employed to investigate superconductivity, as it is unable to detect the diamagnetic state of a SC. The few available XMCD studies have required the deposition of ferromagnetic overlayers.[36] At variance with ferromagnets, SMMs have the advantage of a non-cooperative hysteretic behaviour. Thus, when deposited on SC surfaces, SMMs are a sensitive local tool to monitor magnetic flux distribution of relevance for more complex domain structures, such as those observed in type II or 2D superconductors. For the latter, we can also expect to have a mutual magnetic influence through space, *i.e.* the magnetic flux generated by the SMM can locally affect the SC. Particularly relevant for the scientific community would be the investigation of the SMM/SC interface by scanning probe techniques with magnetic sensing capabilities and high spatial resolution.

Equally relevant is the possibility to locally switch the SMM magnetization dynamics biasing the magnetic field at the superconductor transition. This effect is highly interesting for quantum information technologies and is expected to be particularly pronounced for lanthanoid-based SMMs, whose magnetization relaxation time can be enhanced by several orders of magnitude[37] in zero field.

Data Availability

Experimental data used to draw Fig. 3a-d and Fig.4a are included with the manuscript as source data. Additional data such as STM images, simulated hysteresis curves and DFT results are available from the authors on request.

Code Availability

The code to compute magnetic hysteresis using the kinetic Monte Carlo method is available from the ETH Zurich Data Archive: http://doi.org/10.5905/ethz-XXXXX (final doi to be inserted in proofs).

References

1. Linder, J. & Robinson, J. W. A. Superconducting spintronics. *Nat. Phys.* **11**, 307–315 (2015).
2. Franke, K. J., Schulze, G. & Pascual, J. I. Competition of Superconducting Phenomena and Kondo Screening at the Nanoscale. *Science* **332**, 940–944 (2011).
3. Malavolti, L. *et al.* Tunable Spin-Superconductor Coupling of Spin ½ Vanadyl-Phthalocyanine Molecules. *Nano Lett.* **18**, 7955–7961 (2018).
4. Heinrich, B. W., Pascual, J. I. & Franke, K. J. Single magnetic adsorbates on s-wave superconductors. *Prog. Surf. Sci.* **93**, 1–19 (2018).
5. Kezilebieke, S., Dvorak, M., Ojanen, T. & Liljeroth, P. Coupled Yu–Shiba–Rusinov States in Molecular Dimers on $NbSe_2$. *Nano Lett.* **18**, 2311–2315 (2018).
6. Farinacci, L. *et al.* Tuning the Coupling of an Individual Magnetic Impurity to a Superconductor: Quantum Phase Transition and Transport. *Phys. Rev. Lett.* **121**, 196803 (2018).
7. Heinrich, B. W., Braun, L., Pascual, J. I. & Franke, K. J. Protection of excited spin states by a superconducting energy gap. *Nat. Phys.* **9**, 765–768 (2013).
8. Gatteschi, D., Sessoli, R. & Villain, J. *Molecular Nanomagnets*. **54**, (Oxford University Press 2006, 2006).
9. Sanvito, S. *et al.* Molecular spintronics. *Chem. Soc. Rev.* **40**, 3336–3355 (2011).
10. Godfrin, C. *et al.* Operating Quantum States in Single Magnetic Molecules: Implementation of Grover's Quantum Algorithm. *Phys. Rev. Lett.* **119**, 187702 (2017).
11. Cornia, A., Mannini, M., Sessoli, R. & Gatteschi, D. Propeller-Shaped Fe_4 and Fe_3M Molecular Nanomagnets: A Journey from Crystals to Addressable Single Molecules. *Eur. J. Inorg. Chem.* **2019**, 552–568 (2019).
12. Mannini, M. *et al.* Magnetic memory of a single-molecule quantum magnet wired to a gold surface. *Nat. Mater.* **8**, 194–197 (2009).
13. Mannini, M. *et al.* Quantum tunnelling of the magnetization in a monolayer of oriented single-molecule magnets. *Nature* **468**, 417–421 (2010).
14. Malavolti, L. *et al.* Magnetic Bistability in a Submonolayer of Sublimated Fe_4 Single-Molecule Magnets. *Nano Lett.* **15**, 535–541 (2015).
15. Totaro, P. *et al.* Tetrairon(III) Single-Molecule Magnet Monolayers on Gold: Insights from ToF-SIMS and Isotopic Labeling. *Langmuir* **30**, 8645–8649 (2014).

16. Margheriti, L. *et al.* X-Ray Detected Magnetic Hysteresis of Thermally Evaporated Terbium Double-Decker Oriented Films. *Adv. Mater.* **22**, 5488–5493 (2010).
17. Serrano, G. *et al.* Magnetic bistability of TbPc$_2$ submonolayer on a graphene/SiC(0001) conductive electrode. *Nanoscale* **10**, 2715–2720 (2018).
18. Wäckerlin, C. *et al.* Giant Hysteresis of Single-Molecule Magnets Adsorbed on a Nonmagnetic Insulator. *Adv. Mater.* **28**, 5195–5199 (2016).
19. Studniarek, M. *et al.* Understanding the Superior Stability of Single-Molecule Magnets on an Oxide Film. *Adv. Sci.* **6**, 1901736 (2019).
20. Carretta, S. *et al.* Intra- and inter-multiplet magnetic excitations in a tetrairon(III) molecular cluster. *Phys. Rev. B* **70**, 214403 (2004).
21. Erler, P. *et al.* Highly Ordered Surface Self-Assembly of Fe$_4$ Single Molecule Magnets. *Nano Lett.* **15**, 4546–4552 (2015).
22. Gragnaniello, L. *et al.* Uniaxial 2D Superlattice of Fe$_4$ Molecular Magnets on Graphene. *Nano Lett.* **17**, 7177–7182 (2017).
23. Paschke, F., Erler, P., Enenkel, V., Gragnaniello, L. & Fonin, M. Bulk-Like Magnetic Signature of Individual Fe$_4$H Molecular Magnets on Graphene. *ACS Nano* **13**, 780–785 (2019).
24. Chanin, G. & Torre, J. P. Critical-Field Curve of Superconducting Lead. *Phys. Rev. B* **5**, 4357–4364 (1972).
25. Rajaraman, G., Caneschi, A., Gatteschi, D. & Totti, F. A periodic mixed gaussians–plane waves DFT study on simple thiols on Au(111): adsorbate species, surface reconstruction, and thiols functionalization. *Phys. Chem. Chem. Phys.* **13**, 3886 (2011).
26. Ninova, S. *et al.* Valence electronic structure of sublimated Fe$_4$ single-molecule magnets: an experimental and theoretical characterization. *J. Mater. Chem. C* **2**, 9599–9608 (2014).
27. Kappler, J.-P. *et al.* Ultralow-temperature device dedicated to soft X-ray magnetic circular dichroism experiments. *J. Synchrotron Rad* **25**, 1727–1735 (2018).
28. Mannini, M. *et al.* Spin Structure of Surface-Supported Single-Molecule Magnets from Isomorphous Replacement and X-ray Magnetic Circular Dichroism. *Inorg. Chem.* **50**, 2911–2917 (2011).
29. Cornia, A. *et al.* Energy-barrier enhancement by ligand substitution in tetrairon(III) single-molecule magnets. *Angew. Chem. Int. Ed.* **43**, 1136–1139 (2004).
30. Vergnani, L. *et al.* Magnetic Bistability of Isolated Giant-Spin Centers in a Diamagnetic Crystalline Matrix. *Chem. Eu. J.* **18**, 3390–3398 (2012).
31. Kumar, P. *et al.* Origin and Reduction of 1/f Magnetic Flux Noise in Superconducting Devices. *Phys. Rev. Appl.* **6**, 041001 (2016).

32. Wang, H. *et al.* Candidate Source of Flux Noise in SQUIDs: Adsorbed Oxygen Molecules. *Phys. Rev. Lett.* **115**, 077002 (2015).

33. Poole, C. P., Farach, H. A., Creswick, R. J. & Prozorov, R. *Superconductivity*. (Elsevier Science, 2014).

34. Prozorov, R. Equilibrium Topology of the Intermediate State in Type-I Superconductors of Different Shapes. *Phys. Rev. Lett.* **98**, 257001 (2007).

35. Prozorov, R., Giannetta, R. W., Polyanskii, A. A. & Perkins, G. K. Topological hysteresis in the intermediate state of type-I superconductors. *Phys. Rev. B* **72**, 212508 (2005).

36. Ruoß, S., Stahl, C., Weigand, M., Schütz, G. & Albrecht, J. High-resolution dichroic imaging of magnetic flux distributions in superconductors with scanning x-ray microscopy. *Appl. Phys. Lett.* **106**, 022601 (2015).

37. Car, P.-E. *et al.* Giant field dependence of the low temperature relaxation of the magnetization in a dysprosium(III)–DOTA complex. *Chem. Commun.* **47**, 3751-3753 (2011).

Methods

Synthesis and preparation of the hybrid interface

Fe_4SMe (isolated in crystalline form as the hemidiethylether solvate) was synthesized and chemically characterized at the University of Modena and Reggio Emilia. A detailed description of the synthetic procedure and selected characterization data are provided in the Supplementary Information, Note 1.

The Pb(111) crystal (disk-shaped, 4 mm of diameter and 3 mm thickness) was purchased from the Surface Preparation Laboratory – SPL (Zaandam, NL). Surface preparation and characterization were performed at the University of Florence. The Pb(111) surface was prepared by cycles of Ar sputtering (1 keV energy) and annealing at 470 K in Ultra High Vacuum (UHV) and controlled by XPS and STM measurements. Molecular deposition was performed by thermal sublimation in UHV. Crystals of Fe_4SMe were crushed into a powder and inserted in a resistively heated quartz crucible. The powder was purified by repeated thermal treatment cycles to remove solvent residuals.

The deposition of the Fe_4SMe sub-monolayer on lead was carried out in controlled atmosphere ($P < 10^{-10}$ mbar) at a temperature of about 490 K measured by a K-thermocouple in direct contact with the powder. The deposition rate was monitored by a quartz crystal microbalance placed in front of the crucible.

Experimental characterization

The STM characterization was carried out by an Omicron Variable-Temperature STM, where the sample was cooled down to 30 K by a liquid helium flux. Diffraction pattern images were acquired by Omicron Spectaleed rear view LEED optics. XPS characterization was performed with a micro-focused monochromatic Al K-alpha radiation source (hν = 1486.7 eV), model SPECS XR-MS Focus 600, and a multichannel detector electron analyser, model SPECS Phoibos 150 1DLD. XPS spectra were recorded in normal emission with the X-ray source mounted at an angle of 54.44° with respect to the analyser and using a pass energy of 40 eV. Spectra were calibrated using the $Pb4f_{7/2}$ component at 136.9eV.[38] The spectra were fitted using a linear background and single peak components were deconvoluted by a mixed Gaussian and Lorentzian function. Spectra were analysed using the CasaXPS software. UPS characterization was carried out using a He (II) line (with an energy of 40.8 eV) by non-monochromatized gas discharge lamp (VG Scientific 22-101). The analyser was the same used for XPS with a pass energy of 10 eV and an entrance and an exit slit of 3×20 mm. A fixed bias of −30 V was applied to the sample to ensure the detection of all the photoelectrons.

XAS, XMCD, and XNLD experiments were carried out at the DEIMOS beamline (SOLEIL synchrotron, France) using the novel Dichro50 setup working in the mK temperature range.[27] Samples were prepared in Florence following the above-reported procedures and transferred to the beamline facilities using a UHV suitcase equipped with a D100 SAES Nextorr Neg - Ion Combination Pump that guaranteed a pressure $P < 10^{-10}$ mbar during the transport. All the steps from sample preparation to synchrotron measurements were accomplished without breaking the vacuum connection ($P < 10^{-9}$ mbar). XAS spectra were acquired in Total Electron Yield (TEY) mode.[39] The XMCD signals, calculated as the difference $\sigma^- - \sigma^+$, were normalized with respect to the L_3 edge-jump of $(\sigma^+ + \sigma^-)/2$ and expressed in percentage.[15] The XNLD signals were normalized with respect to the L_3 edge-jump of the isotropic spectrum (*i.e.* $1/3\ \sigma^V + 2/3\ \sigma^H$ when □ = 45°)[40] and expressed in percentage.

Computational Methods

All the periodic density functional theory calculations (pDFT) were performed with CP2K quantum chemistry software.[41] Gaussian plane waves formalism (GPW)[42] was employed to solve the eigenvalue problem. Norm-conserving Goedecker-Tetter Hutter (GTH) pseudopotentials,[43] along with double zeta basis set with polarization functions (DZVP-MOLOPT-SR)[43] were employed for all atoms. The cut-off energy for the plane-wave auxiliary basis set was set to 400 Ry. Meta-GGA RevPBE functional[44,45] with empirical dispersion correction RVV10[46] was used throughout all the calculations. Constant electronic smearing of 1500 K was applied to consider the metal character of the slab. The threshold for the atomic forces during the geometry optimization runs was set to 0.003 Hartree/ a_0, where a_0 is the Bohr radius (1 Hartree/a_0 = 8.2387234983(12) × 10^{-8} N). During the single SCF step the convergence criterion was set to a wavefunction gradient of 1×10^{-6}.

Two different kinds of geometry optimizations were performed: the optimization of a single Fe_4SMe molecule (A) and the optimization of the adduct made by three Fe_4SMe molecules (B). The dimensions of the periodic cell were set to 31.5 × 30.3 × 60 Å for A and to 45.5 × 42.42 × 60 Å for B, in order to avoid interactions between replicas along both x and y directions and between slabs along the z direction. The Pb(111) surface was modelled with three slabs, each one made of 9 × 10 Pb atoms for A and of 14 × 13 for B. The bottom layer was kept fixed during all geometry optimizations, while the others were left free to relax. Such Pb(111) surface model was previously validated in Ref. 3, according to Ref. 47.

The starting guess geometry for optimization B was the final geometry obtained from optimization A. The latter was indeed replicated by a rigid rotation of 120° and 240° along the normal to the surface.

A total spin value corresponding to a broken symmetry state[48] with $m_S = 5$ was chosen, with the central Fe^{3+} ion antiferromagnetically coupled with the three peripheral ones.

References

38. Bozack, M. J. & Bryant, K. W. Elemental Lead by XPS. *Surf. Sci. Spectra* **1**, 324–327 (1992).
39. Nakajima, R., Stöhr, J. & Idzerda, Y. U. Electron-yield saturation effects in *L* -edge x-ray magnetic circular dichroism spectra of Fe, Co, and Ni. *Phys. Rev. B* **59**, 6421–6429 (1999).
40. Brouder, C. Angular dependence of X-ray absorption spectra, *J. Phys. Condens. Matter.* **2,** 701–738 (1990).
41. Hutter, J., Iannuzzi, M., Schiffmann, F. & VandeVondele, J. cp2k: atomistic simulations of condensed matter systems. *Wiley Interdiscip. Rev. Comput. Mol. Sci.* **4**, 15–25 (2014).
42. Lippert, B. G. & parrinello, J. H. and M. A hybrid Gaussian and plane wave density functional scheme. *Mol. Phys.* **92**, 477–488 (1997).
43. Krack, M. Pseudopotentials for H to Kr optimized for gradient-corrected exchange-correlation functionals. *Theor. Chem. Acc.* **114**, 145–152 (2005).
44. Zhang, Y. & Yang, W. Comment on "Generalized Gradient Approximation Made Simple". *Phys. Rev. Lett.* **80**, 890–890 (1998).
45. Perdew, J. P., Burke, K. & Ernzerhof, M. Generalized Gradient Approximation Made Simple. *Phys. Rev. Lett.* **77**, 3865–3868 (1996).
46. Sabatini, R., Gorni, T. & de Gironcoli, S. Nonlocal van der Waals density functional made

simple and efficient. *Phys. Rev. B* **87**, 041108 (2013).

47. Caneschi, A., Gatteschi, D. & Totti, F. Molecular magnets and surfaces: A promising marriage. A DFT insight. *Coord. Chem. Rev.* **289–290**, 357–378 (2015).
48. Bencini, A. & Totti, F. A Few Comments on the Application of Density Functional Theory to the Calculation of the Magnetic Structure of Oligo-Nuclear Transition Metal Clusters. *J. Chem. Theory Comput.* **5**, 144–154 (2009).

Acknowledgments

We acknowledge SOLEIL for provision of synchrotron radiation facilities. We thank Philippe Ohresser, Jean Paul Kappler and Loïc Joly for the realization of the ULT-XMCD setup and for assistance in using the DEIMOS beamline. The European COST Action CA15128 MOLSPIN, the Quantera ERA-NET Co-fund project SUMO, and the FET Open Femtoterabyte project are acknowledged for financial support. Italian MIUR, through PRIN project QCNaMoS (2015-HYFSRT) and Progetto Dipartimenti di Eccellenza 2018-2022 (ref B96C1700020008), and Fondazione Ente Cassa di Risparmio di Firenze are also acknowledged for financial support.

Author contribution

GS, LP, ALS, GC, and LM performed the synchrotron experiments with the assistance of EO, PS, and MM. LP, GS, BC, and ALS prepared and characterized the hybrid interface. MB and FT performed the DFT studies. FP and AC prepared and structurally characterized the Fe_4SMe SMM. RS, ALB, and AC performed its bulk phase magnetic characterization. AV developed the kinetic Monte Carlo method and contributed with GS and RS to the simulation of the XMCD magnetic data. AC, FT, MM, and RS supervised the activities of the project. All authors contributed to the discussion and preparation of the manuscript.

Competing Interests

The authors declare no competing interests.

Captions to Figures and Extended Data

Figure 1 (a) Structure of Fe_4SMe in the crystalline phase (atom colour code: green = Fe, red = O, yellow = S, brown = C). For clarity, the carbon backbone is drawn using capped sticks. Hydrogen atoms are not shown. Arrows indicate the arrangement of spin vectors in the ground $S = 5$ state. The tripodal ligand with the CH_2SMe substituent is depicted in the rectangular panel (white capped sticks = H). (b) Stable structure of Fe_4SMe on Pb(111) calculated by DFT, showing the deviation of the magnetic easy axis (C_3) from the surface normal (*n*). The computed electron density difference is also shown (the surfaces are drawn for a value of 0.0025 e bohr^{-3}). Cyan and orange colours correspond to reduced and increased electron densities, respectively, as compared with non-interacting components (Pb surface and Fe_4SMe).

Figure 2 (a-c) STM images (V_{bias}=2.6 V, I_{tunnel}=10 pA) of the Fe_4SMe sub-monolayer on Pb(111) at different magnifications. A portion of clean Pb(111) surface is visible in the top-right side of panel a. The dotted triangle in panel b highlights the molecular superstructure; a single molecular unit is indicated in shadow. (d) Simulated STM image of three molecules in the layer. Each Fe_4SMe molecule appears as two main spots aligned with the projection of the easy axis, which is marked with a pink line in panels c and d; the brighter and dimmer spots correspond to the CH_2SMe group pointing outward and to a tert-butyl group of the topmost dpm$^-$ ligand, respectively. The second CH_2SMe group cannot be directly identified from the experimental images, but it lies just beneath the latter spot. Additional lateral spots can be attributed to the surrounding envelope of dpm$^-$ ligands.

Figure 3 XMCD (a) and XNLD (b) spectra of Fe_4SMe on Pb(111) at the Fe $L_{2,3}$ edges. XMCD signal (green) was obtained by recording XAS spectra with positive (red) and negative (blue) circular light polarization at T = 220 mK, B = 3 T and $\theta = 0°$. XNLD signal (cyan) was obtained from the difference of the XAS spectra recorded with vertical (violet) and horizontal (orange) linear light polarization at 220 mK, 3 T and $\theta = 45°$. Temperature (c) and angular (d) dependence of experimental (top) and simulated (bottom) hysteresis loops. In the temperature dependence, experimental data were recorded by monitoring the XMCD signal at 709.2 eV at different temperatures (see legend) and normal incidence while sweeping the field continuously between -1.5/+1.5 T for right and left circular polarizations with a sweep rate v_{sweep} = 0.01 T/s. In the angular dependence, experimental curves were recorded at θ = 0° (blue) and θ = 45° (dark red) at 220 mK. Curves were simulated using the kinetic Monte Carlo approach (see text). In the simulations, the magnetic easy axes were arranged on the surface of a cone (a magnified version of the inset in panel d is shown in Extended Data Fig. 3d). Assuming a continuous distribution on the cone surface or 12 discrete orientations of the easy-axis projection, as suggested by STM analysis (see Extended Data Fig. 2a), yields virtually identical simulated curves. Thin (thick) lines and empty (filled) symbols represent upfield (downfield) hysteresis branches. Arrows help to visualize field scan direction in the simulated curves.

Figure 4 (a) Experimental hysteresis loops acquired close to B_C (0.08T) at θ = 0° and 220 mK: green circles represent the hysteresis acquired by the continuous method (v_{sweep} = 0.0025 T/s) while blue circles refer to spot XMCD values (spot method) recorded after magnetizing the sample at 1 T at each point (detailed explanation is given in the text). Hysteresis loops simulated without considering the SC substrate (black line) and introducing the effect of the SC substrate in the intermediate state (red line) are also shown. Thin (thick) lines and empty (filled) symbols represent upfield (downfield) hysteresis branches. Arrows help to visualize field scan direction in the simulated curves. (b) Scheme of the interaction of SMMs with the SC substrate during the transition to the intermediate state ($|B| < B_C$). For $|B| > B_c$ the molecular spin is aligned along the magnetic field direction; $|B| = B_C$ represents the nominal transition of the type I superconductor to the condensate state. From B_C to zero field, growing substrate areas enter in the complete Meissner state (grey) thus excluding the external magnetic field (B_{loc} =0). Fe_4SMe molecules interacting with these regions feel a magnetic field drop to zero allowing them to bypass the anisotropy barrier via quantum tunnelling. (c) Simulated magnetization curves (upfield branch of the hysteresis loop) for molecules experiencing the SC transition of lead at different B_M and thus at different times in the hysteresis cycle. Simulated hysteresis loop, red line in panel a, was obtained taking into account a convolution of these hystereses (see text).

Extended Data Fig. 1b. (a) TDOS for $Fe_4SMe/Pb(111)$ (purple curve), and pDOS contributions from Fe_4SMe (blue curve) and Pb(111) surface (red curve). A full width at half-maximum (FWHM) $\sigma=0.45$ eV was used. (b) pDOS of atomic contributions in Fe_4SMe calculated on $Fe_4SMe/Pb(111)$ ($\sigma=0.45$ eV). (c) Computed spin density for Fe_4SMe on Pb(111). The surfaces are drawn for a value of 0.001 unpaired e bohr^{-3}. Blue and pink colours correspond to spin up and spin down calculated spin densities, respectively. In the inset, arrows depict the arrangement of the spin vectors in the S = 5 ground state using the same colour code. We notice that a similarly negligible spin delocalization was observed for VOPc deposited on Pb with the vanadyl moiety pointing up, but the spin density increased significantly when the molecule was deformed by the STM tip (see Ref. 3). Here, a similar effect appears very unlikely due to the lack of spin density on atoms close to the Pb surface.

Extended Data Fig. 2a. (a) Magnification of the STM image of Fe_4SMe/Pb(111) in Figure 2a (main text). Orange and pink lines indicate the molecular easy axis projections on the surface. (b) Scheme of the 12 observed orientations of the C_3 molecular axis projection with respect to the crystallographic directions of the Pb(111) surface. The projection of the molecular C_3 axis lies along the main crystallographic directions of Pb(111), orange lines, or at 30° from them, pink lines (only $[\bar{1}10]$ is shown in the STM image for convenience). (c) Low Energy Electron Diffraction (LEED), 60 eV, of the clean Pb(111) crystal used to identify the main crystallographic directions of the substrate, x axis corresponding to the STM scanning direction.

Extended Data Fig. 2b. Magnification of the STM image of Fe_4SMe/Pb(111) in Figure 2b (main text). Single row (1) and double (2) arrangements of the triangular molecular Fe_4SMe superstructures are highlighted.

Extended Data Fig. 2d. Top view of three Fe_4SMe molecules on Pb(111) calculated by DFT; pink lines indicate the projections of molecular C_3 axes. This structure allows to explain the experimental STM topography of Figure 2c.

Extended Data Fig. 3a. XAS and XMCD signal measured at the Fe $L_{2,3}$ edges on Fe_4SMe/Pb(111) at θ=45° (B=3 T, T=220 mK).

Extended Data Fig. 3d. Scheme of the distribution of Fe_4SMe magnetic easy axes on the Pb(111) surface.

Extended Data Fig. 4a. (a) Enlarged version of Figure 4a (main text). (b) Magnetic hysteresis loop (grey spheres) of a monolayer of a Fe_4 complex on a normal metal (here on a gold substrate, see Ref. 27) in the same field region as panel a. The dark grey solid line is the hysteresis loop simulated disregarding the effect of the SC.

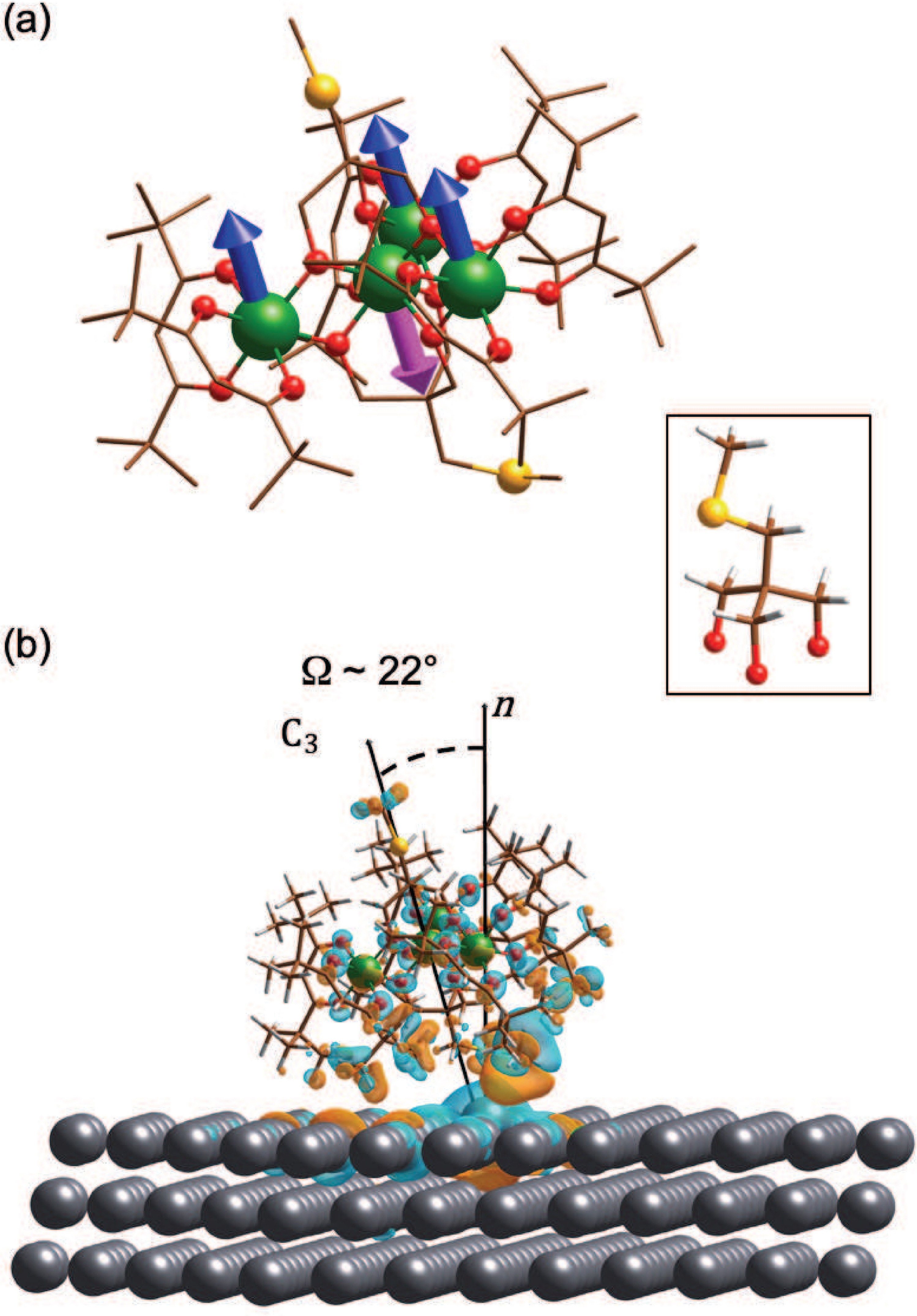
(a)
(b)
Ω ~ 22°
C$_3$
n

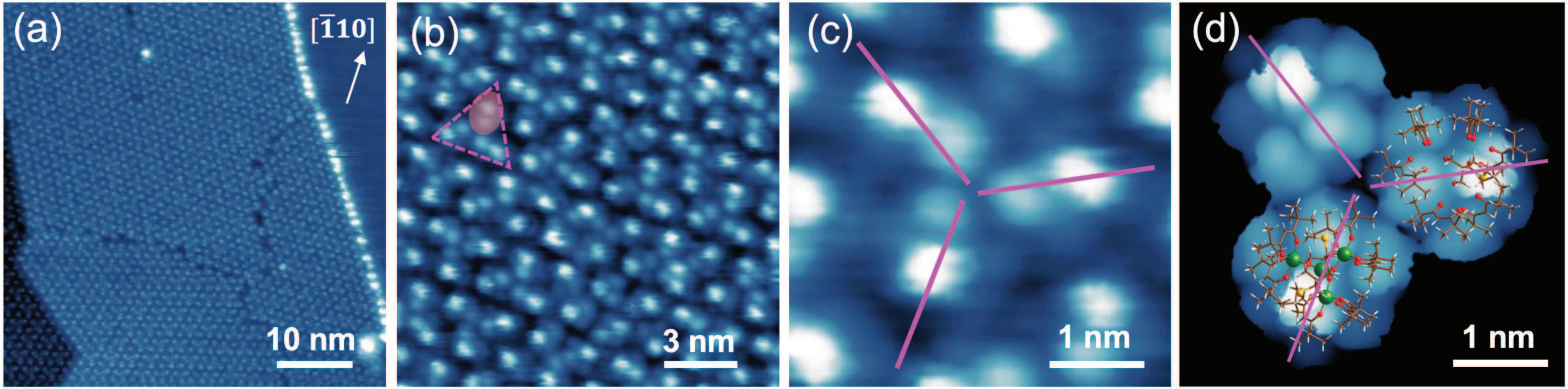
(a)
$[\bar{1}10]$
10 nm
(b)
3 nm
(c)
1 nm
(d)
1 nm

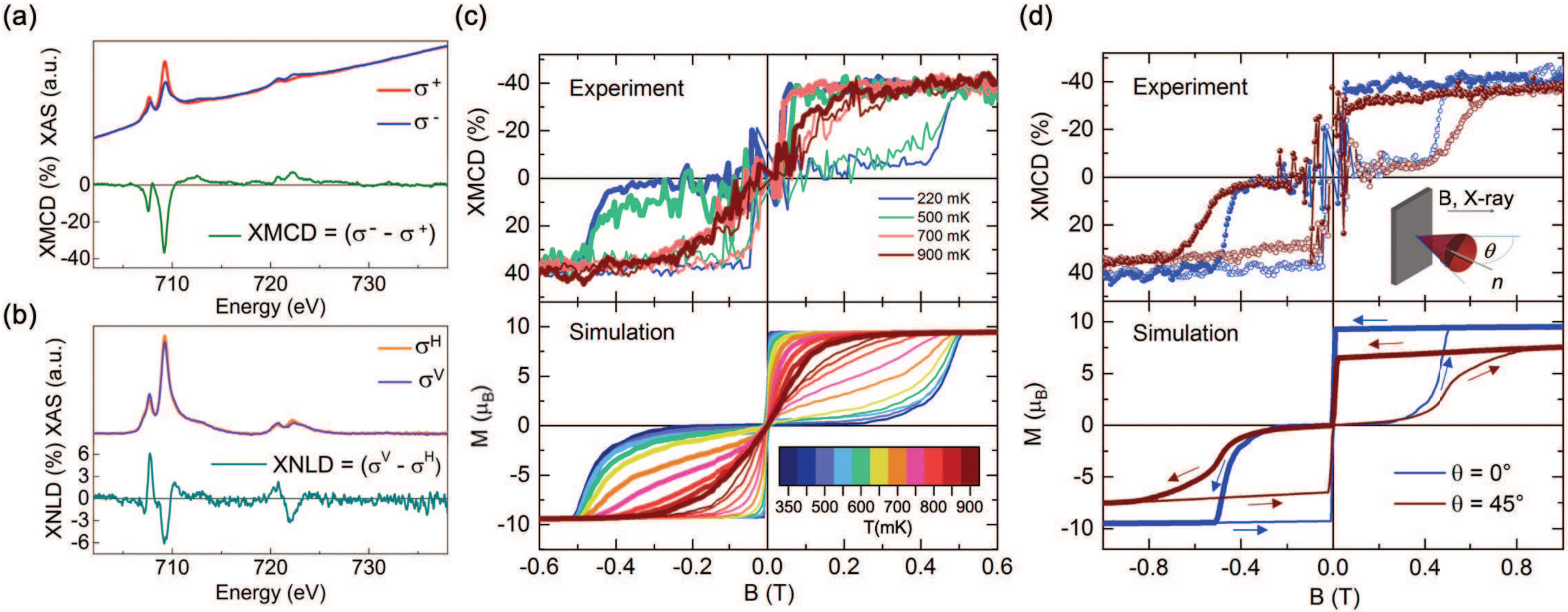
(a)
XMCD (%) XAS (a.u.)
σ+
σ-
0
-20
-40
XMCD = (σ- - σ+)
710
720
730
Energy (eV)
(b)
XNLD (%) XAS (a.u.)
σH
σV
6
3
0
-3
-6
XNLD = (σV - σH)
710
720
730
Energy (eV)
(c)
XMCD (%)
Experiment
-40
-20
0
20
40
220 mK
500 mK
700 mK
900 mK
M (μB)
Simulation
10
5
0
-5
-10
350
500
600
700
800
900
T(mK)
-0.6
-0.4
-0.2
0.0
0.2
0.4
0.6
B (T)
(d)
XMCD (%)
Experiment
-40
-20
0
20
40
B, X-ray
θ
n
M (μB)
Simulation
10
5
0
-5
-10
θ = 0°
θ = 45°
-0.8
-0.4
0.0
0.4
0.8
B (T)

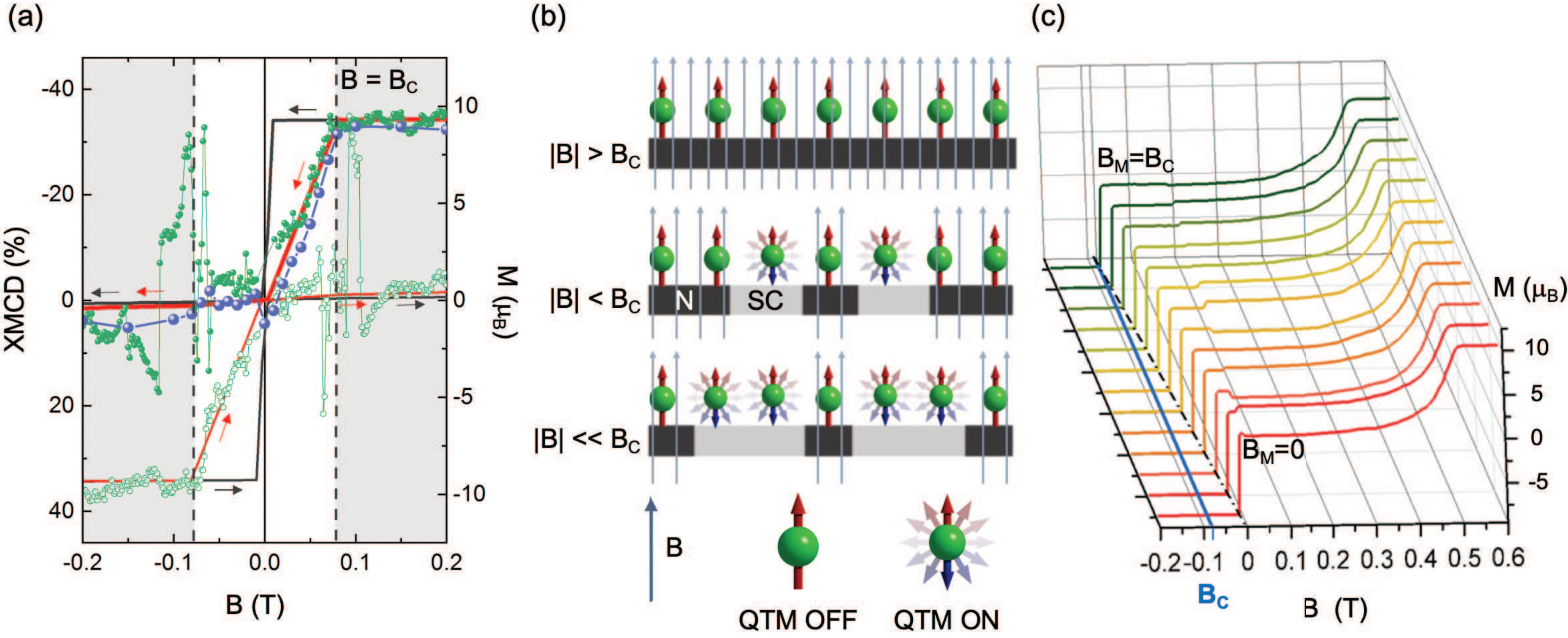
(a)
XMCD (%)
-40
-20
0
20
40
B = B_C
M (μ_B)
10
5
0
-5
-10
-0.2
-0.1
0.0
0.1
0.2
B (T)
(b)
|B| > B_C
|B| < B_C
|B| << B_C
N
SC
B
QTM OFF
QTM ON
(c)
B_M=B_C
B_M=0
M (μ_B)
10
5
0
-5
-0.2
-0.1
0
0.1
0.2
0.3
0.4
0.5
0.6
B_C
B (T)

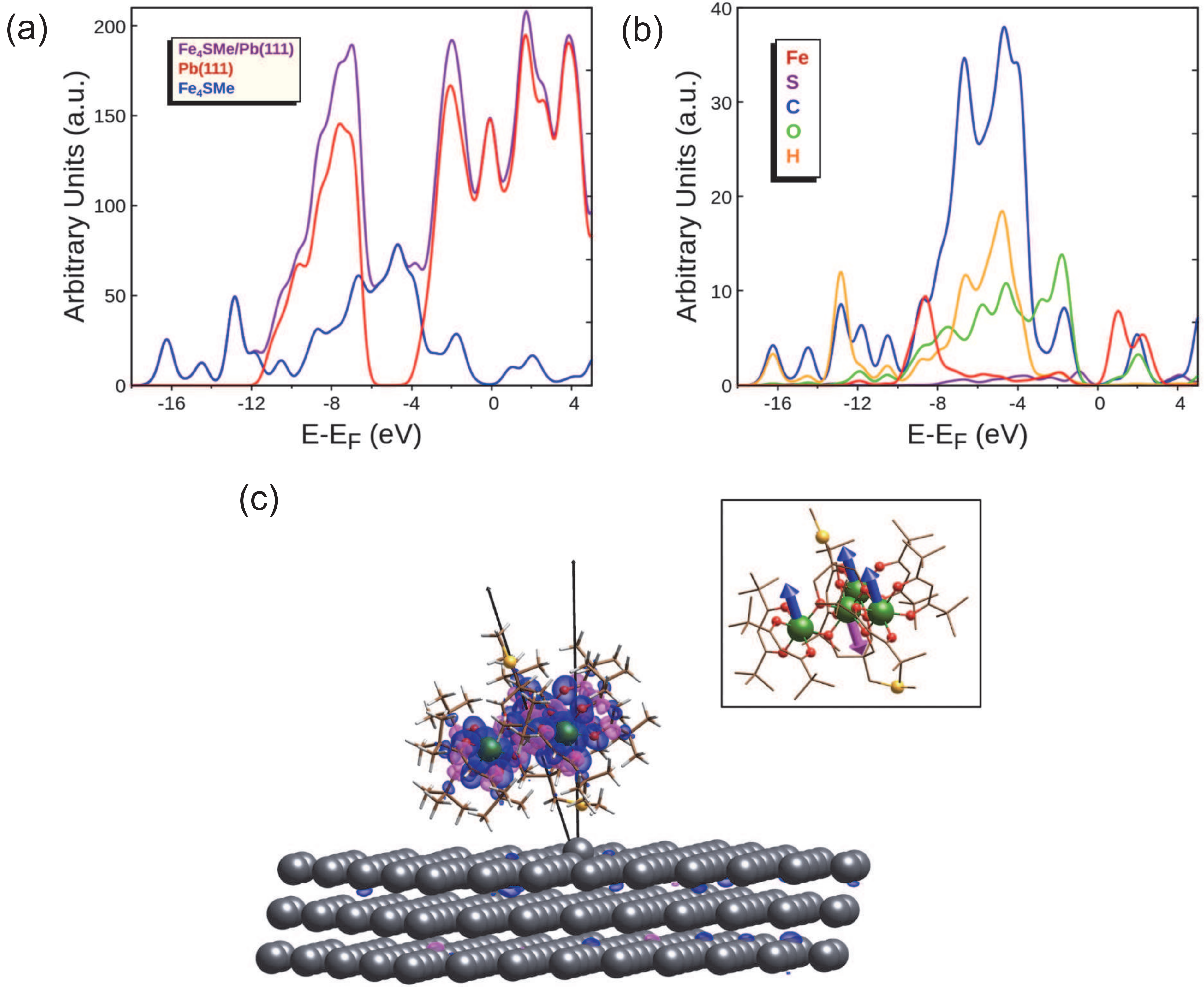
(a)
Arbitrary Units (a.u.)
200
150
100
50
0
-16
-12
-8
-4
0
4
E-E$_F$ (eV)
Fe$_4$SMe/Pb(111)
Pb(111)
Fe$_4$SMe
(b)
Arbitrary Units (a.u.)
40
30
20
10
0
-16
-12
-8
-4
0
4
E-E$_F$ (eV)
Fe
S
C
O
H
(c)

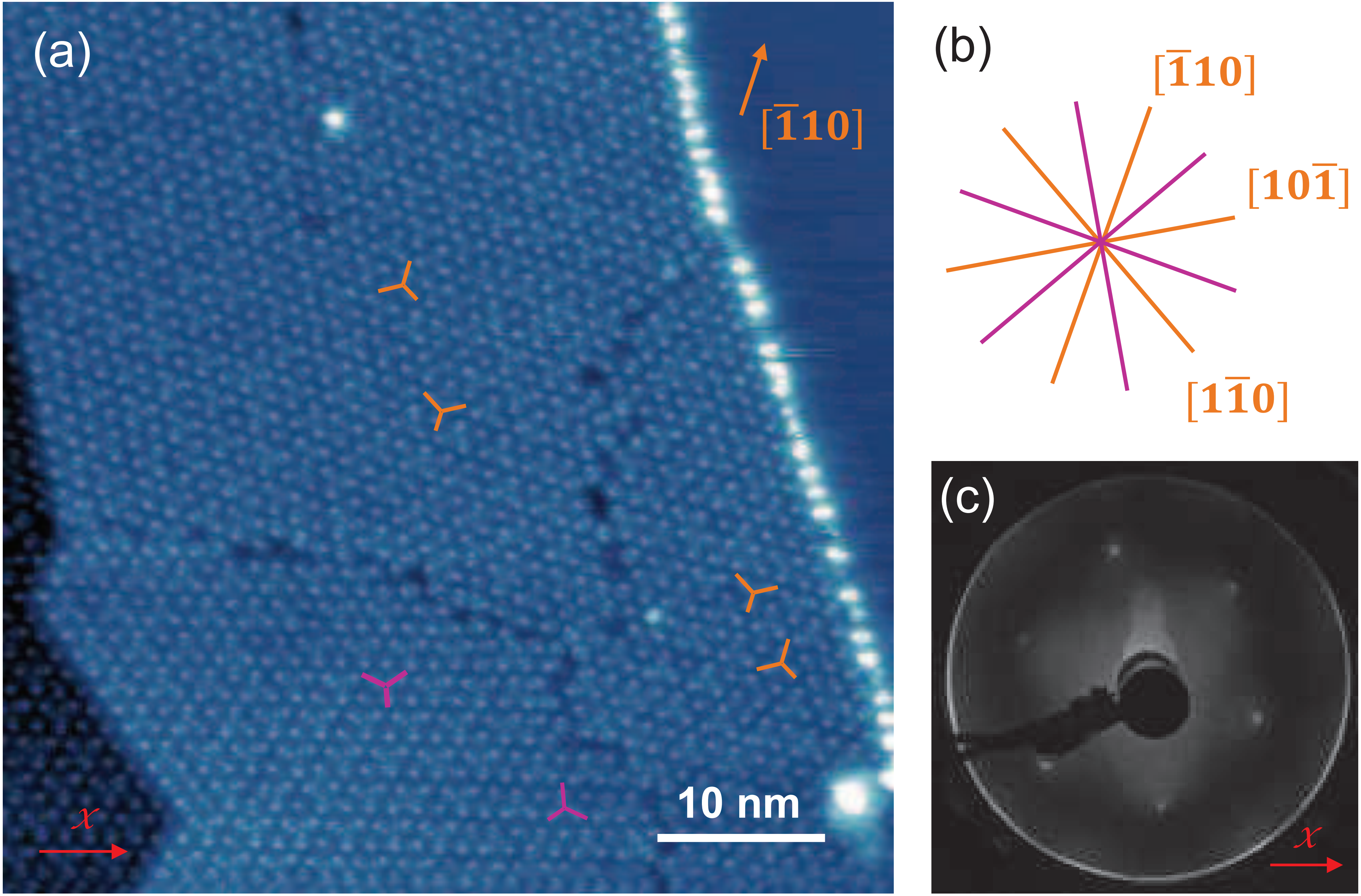
(a)
[$\bar{1}$10]
10 nm
x
(b)
[$\bar{1}$10]
[10$\bar{1}$]
[1$\bar{1}$0]
(c)
x

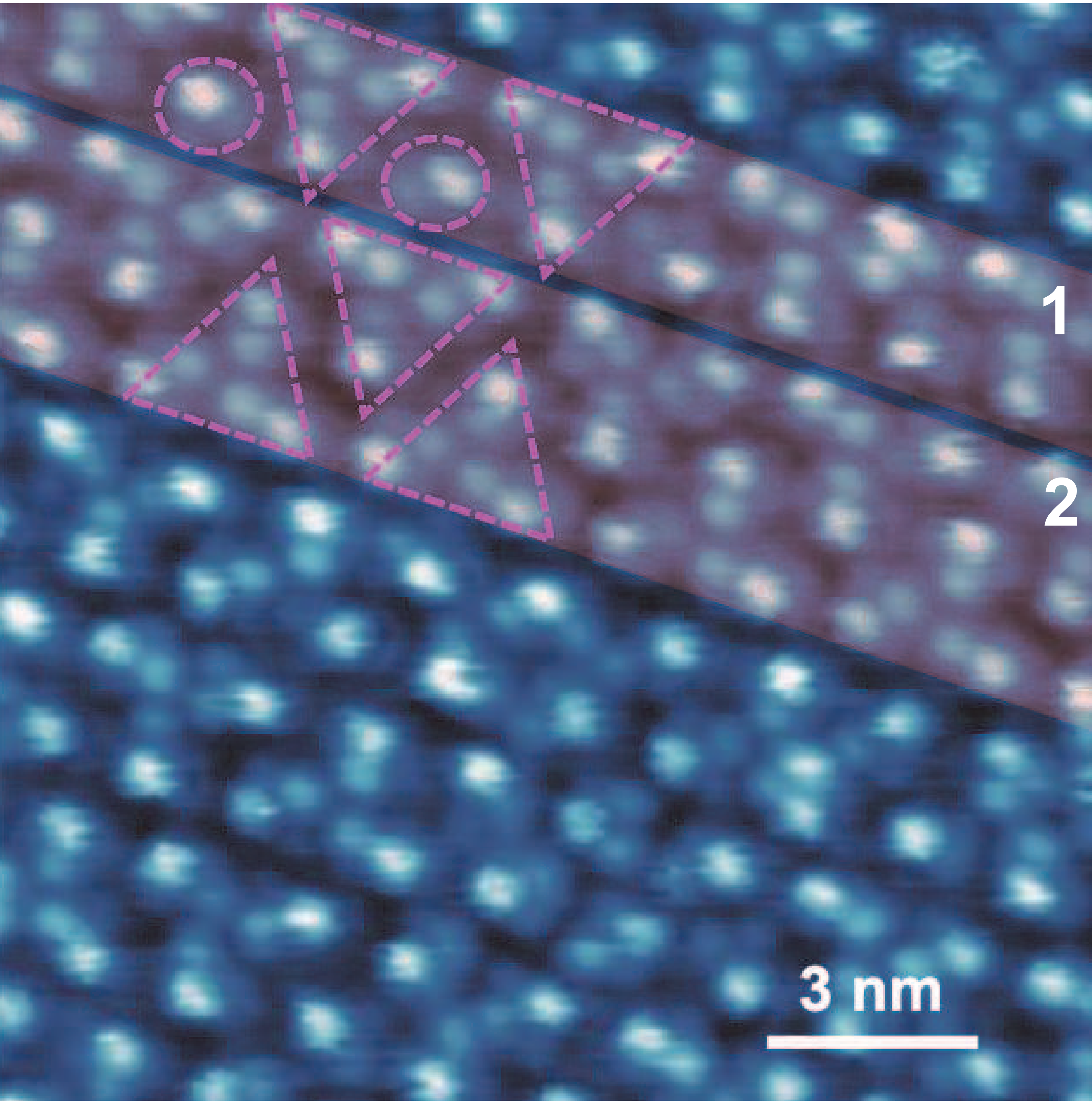
1
2
3 nm

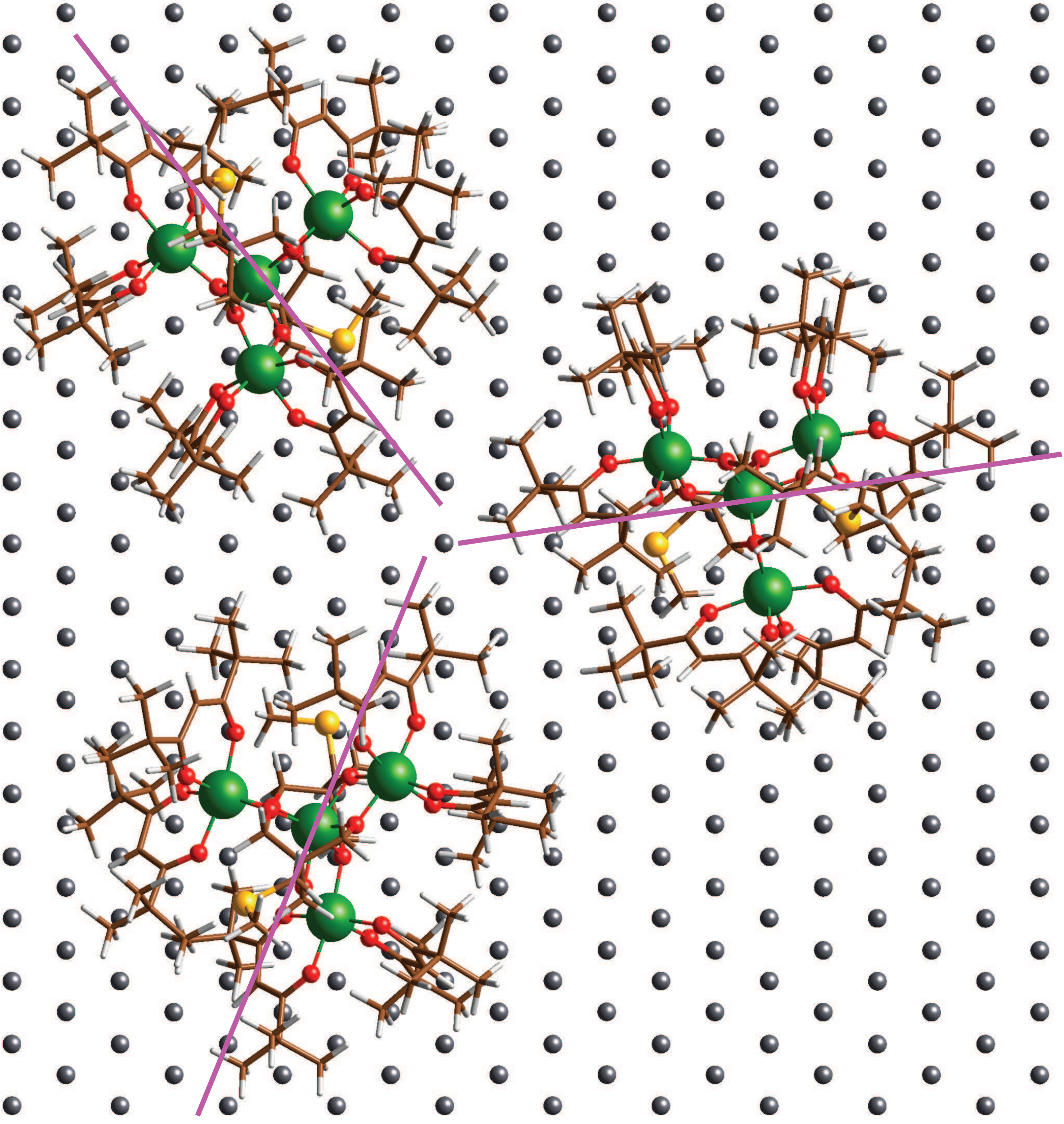

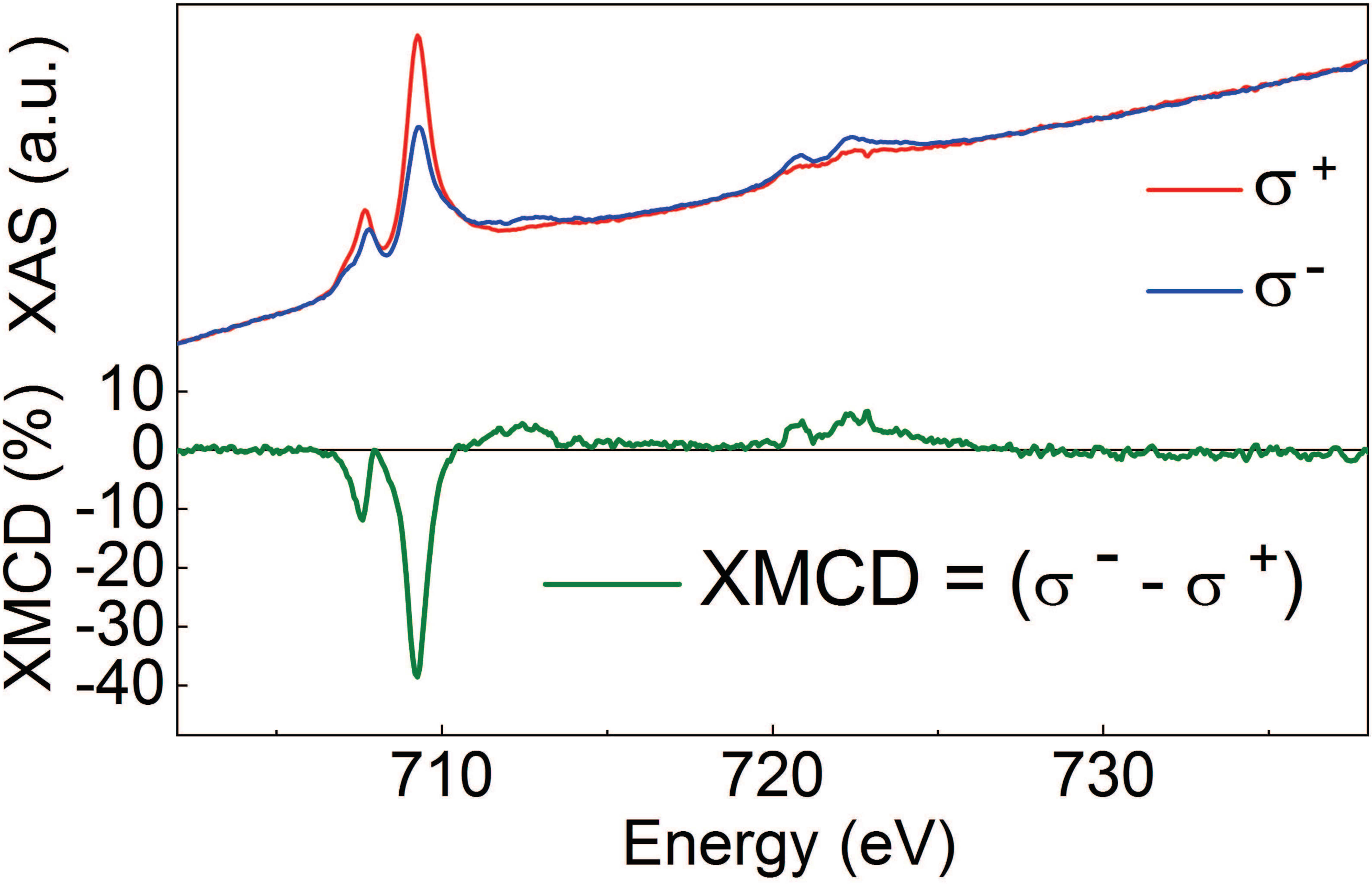
XAS (a.u.)
XMCD (%)
10
0
-10
-20
-30
-40
710
720
730
Energy (eV)
σ^+
σ^-
XMCD = (σ^- - σ^+)

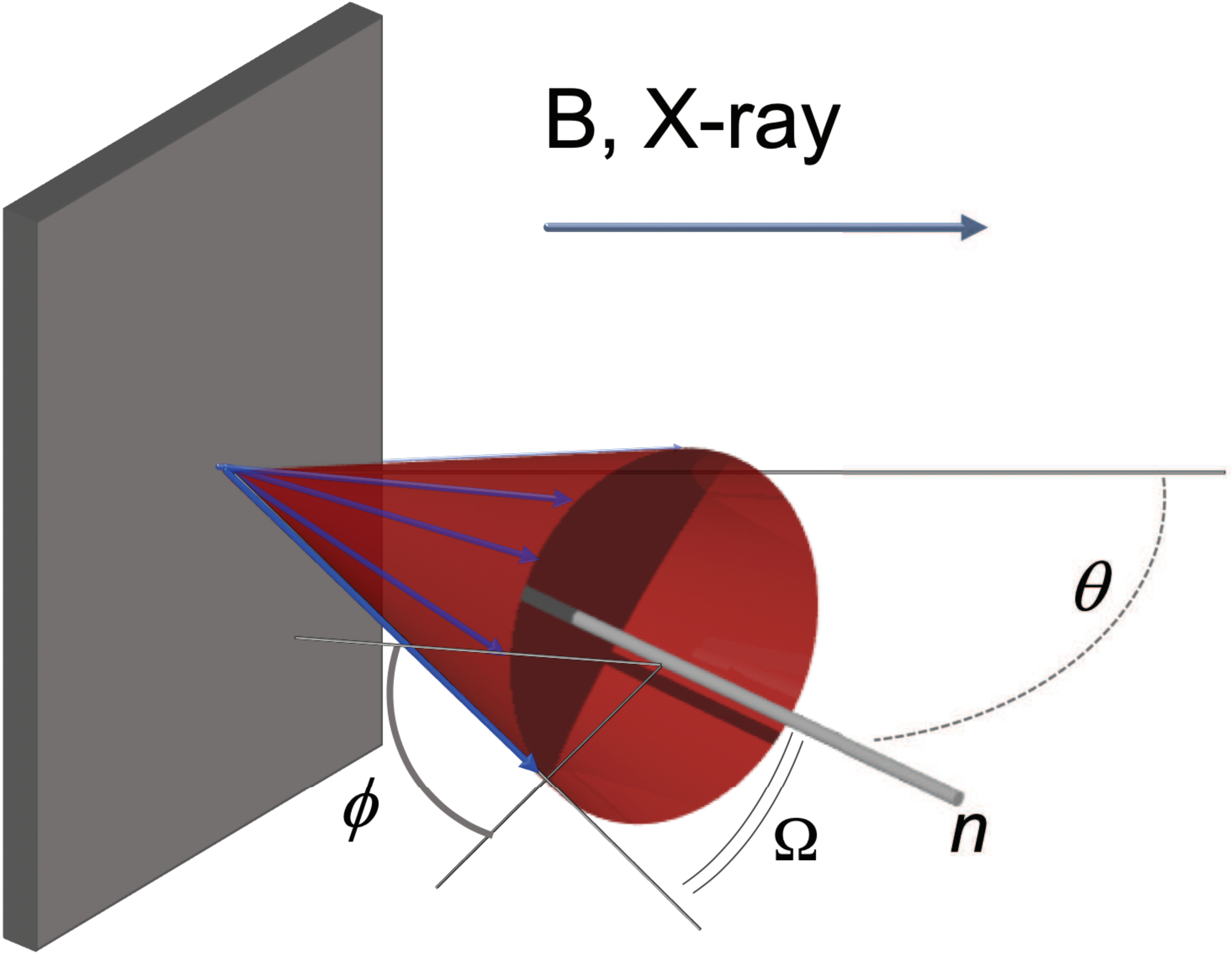
B, X-ray
θ
n
Ω
ϕ

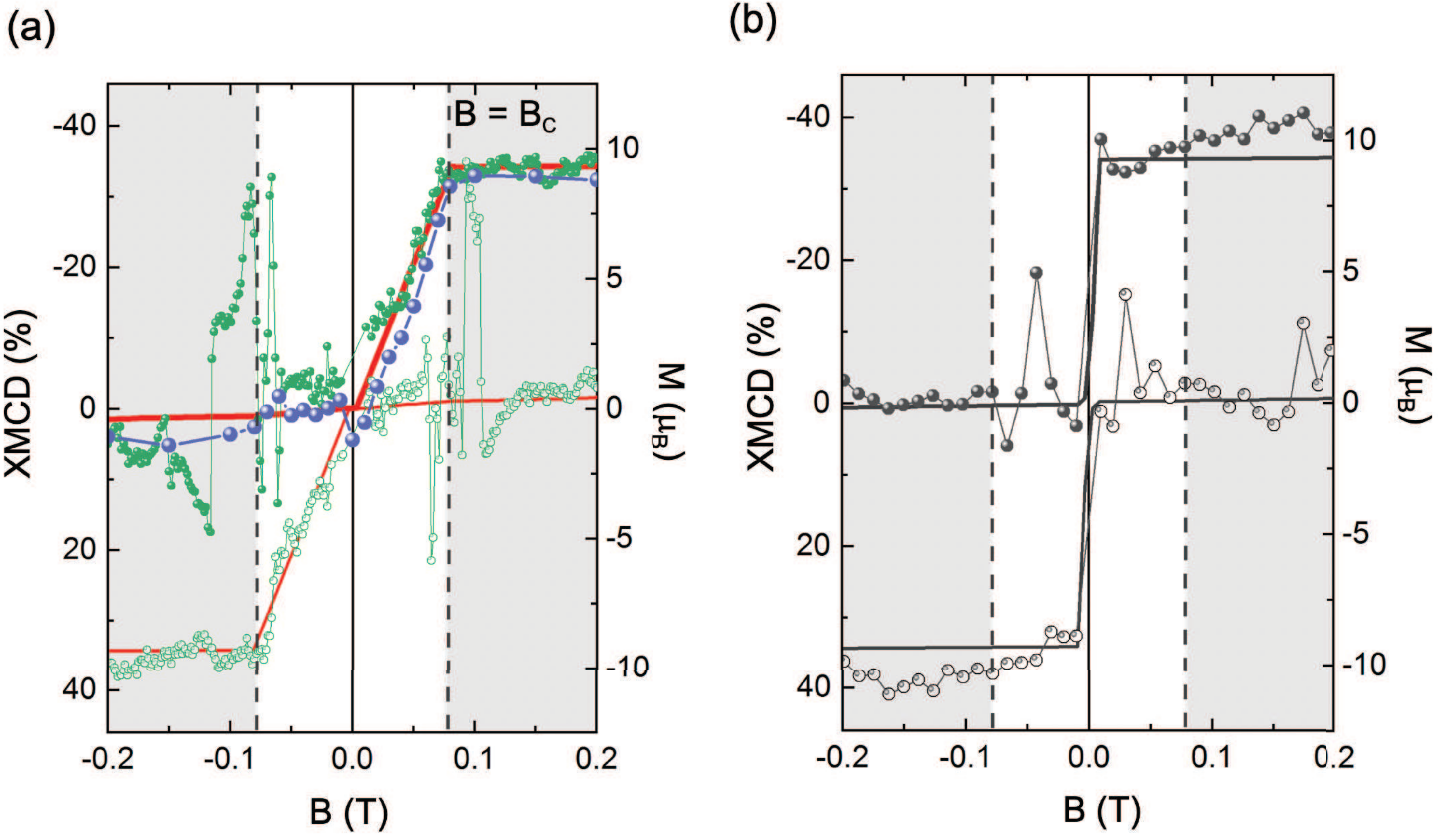
(a)
XMCD (%)
-40
-20
0
20
40
M (μ_B)
10
5
0
-5
-10
B = B_C
-0.2
-0.1
0.0
0.1
0.2
B (T)
(b)
XMCD (%)
-40
-20
0
20
40
M (μ_B)
10
5
0
-5
-10
-0.2
-0.1
0.0
0.1
0.2
B (T)